The Osher Upwind Scheme and its Application to Cosmic Gas Dynamics

AUTHOR(S):

SAWADA, Keisuke; SHIMA, Eiji; MATSUDA, Takuya; INAGUCHI, Takashi

CITATION:

SAWADA, Keisuke ...[et al]. The Osher Upwind Scheme and its Application to Cosmic Gas Dynamics. Memoirs of the Faculty of Engineering, Kyoto University 1986, 48(2): 240-264

ISSUE DATE:

1986-05-17

URL:

http://hdl.handle.net/2433/281325

The Osher Upwind Scheme and its Application to Cosmic Gas Dynamics

By

Keisuke SAWADA*, Eiji SHIMA*, Takuya MATSUDA**
and Takashi INAGUCHI**

(Received December 27, 1985)

Abstract

Details of the second order Osher scheme for the multi-dimensional Euler equation are presented. The adopted method to attain the second order of accuracy differs from the existing second order formulation by Osher. The present method is easy to be implemented and can be applied to other first order upwind schemes.

Two types of numerical integration forms are coded. One is written in the integral form (cell method), and the other is the usual finite-difference form. Both forms work well and can capture strong shocks without any auxiliary artificial damping. The integration form strictly satisfies the flux conservation even on geometrical singular coordinate lines, which inevitably appear in three dimensional calculations with bodies embedded.

Hydrodynamic calculations of the interaction between a stellar wind and an accretion flow are performed to demonstrate the ability of the present method.

1. Introduction

Conventional central difference schemes, such as the Beam and Warming implicit scheme (Beam and Warming, 1976), lack "robustness" in capturing very strong shock waves embedded in the flow field. If one tries to calculate such strong discontinuities by these conventional schemes, excessive artificial damping is required to keep the solution stable, and this damping degrades the resolution of the flow field considerably.

A practical remedy for this situation is to adopt upwind difference schemes. Upwind schemes such as the Godunov scheme (Godunov, 1959), the Osher scheme (Osher and Chakravarthy, 1983) and the Roe scheme (Roe, 1981) have been applied to the Euler equation and show an excellent ability to capture strong shocks. They exploit the characteristic features of the hyperbolic systems of equations.

* Aircraft Engineering Division, Kawasaki Heavy Industries, Kakamigahara, Gifu-Pref., Japan.

** Department of Aeronautical Engineering, Kyoto University, Kyoto, Japan.

However, the spatially first order versions of these upwind schemes are generally highly dissipative. Spurious entropy production may occur even in the smooth regions of the flow field. Such effects can be alleviated by attaining a higher order of spatial accuracy.

Usually, this higher order of accuracy is achieved by estimating the spatial derivatives by the Taylor series expansion up to the desired order. In the smooth region, this procedure works well. In the regions having a large gradient, however, a mechanism to limit the flux must be incorporated. Otherwise some "wiggles" may arise near the discontinuities.

van Leer, in his series of papers (see for example, van Leer, 1979), introduced his flux limiting procedure and developed the second order accurate Godunov scheme. Chakravarthy and Osher (1983) adopted this flux limiting procedure and constructed the second order version of the Osher scheme.

The idea of this flux limiting procedure is simple, but requires a lot of arithmetic operations, and increases the programing complexity. van Albada, van Leer and Roberts (1982) introduced a neat form of the averaging function to obtain practical effects of flux limiting. We adopt this approach of averaging function and construct an alternative form of the second order accurate Osher scheme.

The Osher scheme defines the flux values at the cell interface. This implies that it can be converted easily to the finite volume form (or the integral form) of the numerical scheme, usually called the "cell method". In the cell method, the flux conservation is automatically satisfied even on the geometrically singular coordinate lines and points. This is not the case of the original finite difference form. We develop the cell method version of the second order accurate Osher scheme and apply it to an axisymmetric flow problem occurring in an astrophysical situation.

2. Upwind scheme for linear equations

First, we consider a linear advective equation in a one space dimension

$$q_t+aq_x=0 \tag{2.1}$$

where the suffixes t and x denote the time derivative and the space derivative, respectively.

Assuming the constant a to be positive, we have a conventional upwind scheme with the first order of accuracy as

$$q_j^{n+1}=q_j^n-a\frac{\Delta x}{\Delta t}(q_j^n-q_{j-1}^n)$$

$$q_j^n=q(j\Delta x,\ n\Delta t) \tag{2.2}$$

This upwind scheme is stable for Δt satisfying the well known C. F. L. condition.

The upwind scheme can be extended to the system of linear hyperbolic equa-

tions:

$$\boldsymbol{Q}_t+\boldsymbol{E}_x=0 \tag{2.3}$$

where

$$\boldsymbol{Q}=(q_1,\ q_2,\cdots,\ q_d)^T$$

and $\boldsymbol{E}$ is a flux vector.

This equation can be written in a similar form as (2.1):

$$\boldsymbol{Q}_t+A\boldsymbol{Q}_x=0 \tag{2.4}$$

where $A=\partial\boldsymbol{E}/\partial\boldsymbol{Q}$ is a constant Jacobian matrix. Note that $\boldsymbol{Q}$ is not a vector in physical space, but a vector in d-dimensional state space. We assume that the matrix A has only real eigen-values such that

$$\lambda_1\leqq\lambda_2\leqq\cdots\leqq\lambda_d \tag{2.5}$$

The corresponding right eigen-vectors are denoted as

$$\boldsymbol{R}_1,\ \boldsymbol{R}_2,\cdots,\ \boldsymbol{R}_d$$

where

$$\boldsymbol{R}_i=(r_{i1},\ r_{i2},\cdots,\ r_{id})^T \tag{2.6}$$

They are assumed to be linearly independent.

The matrix A can be diagonalized using the orthogonal matrices P and P^{-1} as

$$D=P^{-1}AP=\begin{pmatrix}\lambda_1 & & 0\\ & \lambda_2 & \\ 0 & & \lambda_d\end{pmatrix} \tag{2.7}$$

where P is composed by the right eigen-vectors as

$$P=\begin{pmatrix}r_{11} & r_{12} & r_{1d}\\ r_{21} & r_{22} & r_{2d}\\ r_{d1} & r_{d2} & r_{dd}\end{pmatrix} \tag{2.8}$$

Multiplication of P^{-1} from the left of Eq. (2.4) yields

$$\boldsymbol{Q}'_t+D\boldsymbol{Q}'_x=0 \tag{2.9}$$

where

$$\boldsymbol{Q}'=P^{-1}\boldsymbol{Q}=(q'_1,\ q'_2,\ \cdots,\ q'_d)^T$$

From this equation we have d uncoupled equations of the form

$$(\partial q_i'/\partial t)+\lambda_i(\partial q_i'/\partial x)=0 \tag{2.10}$$

The upwind difference approximation for these equations can be written as

$$(q'_i)_x=\begin{cases}\dfrac{1}{\Delta x}((q'_i)^n_j-(q'_i)^n_{j-1}) & \text{for } \lambda_i>0\\ \dfrac{1}{\Delta x}((q'_i)^n_{j+1}-(q'_i)^n_j) & \text{for } \lambda_i\leqq 0\end{cases} \tag{2.11}$$

where

$$(q'_i)^n_j=q'_i(j\Delta x,\ n\Delta t)$$

Dividing the matrix D in Eq. (2.7) into two matrices such that

$$D=D^+ +D^- \tag{2.12}$$

where D^+ is a diagonal matrix which has only positive elements, and D^- has only

negative elements. We have the vector forms of Eq. (2.11) as

$$\boldsymbol{Q}'^{n+1}_j=\boldsymbol{Q}'^{n}_j-\frac{\Delta t}{\Delta x}D^+(\boldsymbol{Q}'^{n}_j-\boldsymbol{Q}'^{n}_{j-1})-\frac{\Delta t}{\Delta x}D^-(\boldsymbol{Q}'^{n}_{j+1}-\boldsymbol{Q}'^{n}_j) \tag{2.13}$$

Multiplication of P to the above equation from the left yields

$$\boldsymbol{Q}^{n+1}_j=\boldsymbol{Q}^{n}_j-\frac{\Delta t}{\Delta x}A^+(\boldsymbol{Q}^{n}_j-\boldsymbol{Q}^{n}_{j-1})-\frac{\Delta t}{\Delta x}A^-(\boldsymbol{Q}^{n}_{j+1}-\boldsymbol{Q}^{n}_j) \tag{2.14}$$

where

$$A^+=PD^+P^{-1},\quad A^-=PD^-P^{-1} \tag{2.15}$$

This scheme is known as the Courant-Issacson-Rees upwind scheme (1952). All the schemes for hyperbolic equations which are called "upwind" are the extension of this scheme.

In order to extend this scheme to nonlinear equations, some modifications are added to the scheme. Let us consider a d-dimensional state space (say $\boldsymbol{Q}$-space). Performing the line integration in the $\boldsymbol{Q}$-space, the forward spatial difference term of (2.14) reduces to

$$A^-(\boldsymbol{Q}_{j+1}-\boldsymbol{Q}_j)=\int_{\boldsymbol{Q}_jL}^{\boldsymbol{Q}_{j+1}}A^-d\boldsymbol{Q}=\int_L A^-d\boldsymbol{Q} \tag{2.16}$$

where L is an integration path in the Q-space. The path L can be divided into subpaths in the Q-space as follows:

$$L=L1+L2+\cdots+Ld \tag{2.17}$$

Each subpath is taken to be parallel to the corresponding eigen-vector. According to Eq. (2.15), the value of the integral along each subpath can be written as

$$\int_{Li}A^-d\boldsymbol{Q}=\begin{cases}\displaystyle\int_{Li}Ad\boldsymbol{Q} & \text{for } \lambda_i<0\\ 0 & \text{for } \lambda_i\geqq 0\end{cases} \tag{2.18}$$

since $d\boldsymbol{Q}//\boldsymbol{R}_i$ and

$$A^-\boldsymbol{R}_i=\lambda_i\boldsymbol{R}_i=A\boldsymbol{R}_i \qquad \text{for } \lambda_i<0 \tag{2.19}$$

and

$$A^-\boldsymbol{R}_i=0 \qquad \text{for } \lambda_i\geqq 0 \tag{2.20}$$

If we define the numerical flux function $\boldsymbol{E}$ as

$$\begin{aligned}\boldsymbol{E}_{j+1/2}&=A^+\boldsymbol{Q}_j+A^-\boldsymbol{Q}_{j+1}\\&=A\boldsymbol{Q}_j+\sum_{i=1}^{d}\int_{\substack{Li\\ \lambda_i<0}}Ad\boldsymbol{Q}=A\boldsymbol{Q}_j+\int_{\lambda_i<0}Ad\boldsymbol{Q}\\&=A\boldsymbol{Q}_{j+1}-\int_{\lambda_i\geq 0}Ad\boldsymbol{Q}=\frac{1}{2}(A\boldsymbol{Q}_j+A\boldsymbol{Q}_{j+1})-\frac{1}{2}\int|A|d\boldsymbol{Q}\end{aligned} \tag{2.21}$$

where $|A|=A^+-A^-$, then Eq. (2.14) reduces to

$$\boldsymbol{Q}^{n+1}_j=\boldsymbol{Q}^{n}_j-\frac{\Delta t}{\Delta x}(\boldsymbol{E}_{j+1/2}-\boldsymbol{E}_{j-1/2}) \tag{2.22}$$

3. The first order accurate Osher scheme in one space dimension

Consider a one dimensional Euler equation of the form

$$\boldsymbol{Q}_t+\boldsymbol{E}_x=0 \tag{3.1}$$

where

$$\boldsymbol{Q}=(\rho,\ \rho u,\ e)^T\ \boldsymbol{E}=(\rho u,\ \rho u^2+p,\ (e+p)u))^T \tag{3.2}$$

In the above equation, ρ represents the density, u the velocity, p the pressure and e the specific total energy. The equation of state is

$$P=(\gamma-1)(e-\rho u^2/2) \tag{3.3}$$

in which γ is the ratio of specific heats. The adiabatic sound velocity, c, is defined, for later use, as

$$c=(\gamma p/\rho)^{1/2} \tag{3.4}$$

The equation (3.1) can be written in the quasi-linear form

$$\boldsymbol{Q}_t+A\boldsymbol{Q}_x=0 \tag{3.5}$$

where A is a Jacobian matrix defined by

$$A=\partial\boldsymbol{E}/\partial\boldsymbol{Q}=\begin{pmatrix} 0 & 1 & 0 \\ (\gamma-3)u^2/2 & (3-\gamma)u & \gamma-1 \\ (\gamma-1)u^3-\gamma eu/\rho & \gamma e/\rho+3(1-\gamma)u^2/2 & \gamma u \end{pmatrix} \tag{3.6}$$

The eigen-values of the Jacobian matrix A or 'characteristic velocities' are

$$\lambda_1=u-c,\ \lambda_2=u,\ \lambda_3=u+c \tag{3.7}$$

As a direct extension of Eq. (2.21), we now define the numerical flux function $\boldsymbol{E}$ for Eq. (3.1) as

$$\boldsymbol{E}_{j+1/2}=\boldsymbol{E}(\boldsymbol{Q}_j)+\int_{\lambda_i<0}A d\boldsymbol{Q} \tag{3.8}$$

The integral in Eq. (3.8) can be estimated as follows. Corresponding to each eigen-value λ_i, we can form three linearly independent right eigen-states: $\boldsymbol{R}_1$, $\boldsymbol{R}_2$ and $\boldsymbol{R}_3$. The integration path in the three dimensional state space (again, we call it $\boldsymbol{Q}$-space) can be divided into three subpaths which are parallel to the corresponding right eigen-vectors. An eigen-vector represents a simple wave, which separates two constant states. Across the simple wave, there are two generalized Riemann invariants connecting these two states. Such Riemann invariants are

$$\begin{aligned} &p/\rho^\gamma,\ u+2c/(\gamma-1), && \text{for } \lambda_1=u-c, \\ &p,\ u, && \text{for } \lambda_2=u, \\ &p/\rho^\gamma,\ u-2c/(\gamma-1), && \text{for } \lambda_3=u+c \end{aligned} \tag{3.9}$$

We now define two intermediate states, $\boldsymbol{Q}_{j+1/3}$ and $\boldsymbol{Q}_{j+2/3}$, which are the two connections of the three integration subpaths, to satisfy

$$\int_{L1}A d\boldsymbol{Q}=\boldsymbol{E}(\boldsymbol{Q}_{j+1/3})-\boldsymbol{E}(\boldsymbol{Q}_j) \tag{3.10}$$

$$\int_{L2}A d\boldsymbol{Q}=\boldsymbol{E}(\boldsymbol{Q}_{j+2/3})-\boldsymbol{E}(\boldsymbol{Q}_{j+1/3}) \tag{3.11}$$

and

$$\int_{L3} A d\boldsymbol{Q} = \boldsymbol{E}(\boldsymbol{Q}_{j+1}) - \boldsymbol{E}(\boldsymbol{Q}_{j+2/3}) \tag{3.12}$$

where $\boldsymbol{Q}_j$, $\boldsymbol{Q}_{j+1}$, are variables at the grid points, and Li is an integration path parallel to the eigen-vector $\boldsymbol{R}_i$.

The actual values of these two intermediate points can be computed by using Eqs. (3.7), (3.8) and (3.9) as

$$u_j + 2c_j/(\gamma-1) = u_{j+1/3} + 2c_{j+1/3}/(\gamma-1)$$

$$p_j/\rho_j^\gamma = p_{j+1/3}/\rho_{j+1/3}^\gamma \tag{3.13}$$

$$p_{j+1/3} = p_{j+2/3},\quad u_{j+1/3} = u_{j+2/3} \tag{3.14}$$

$$u_{j+2/3} - 2c_{j+2/3}/(\gamma-1) = u_{j+1} - 2c_{j+1}/(\gamma-1),$$

$$p_{j+2/3}/\rho_{j+2/3}^\gamma = p_{j+1}/\rho_{j+1}^\gamma \tag{3.15}$$

Note that our integration path from $\boldsymbol{Q}_j$ to $\boldsymbol{Q}_{j+1}$ is $L1$, $L2$ and $L3$. On the other hand, Osher and Chakravarthy (1983) took the path $L3$, $L2$ and $L1$. The relation between these two paths are discussed by Pandolfi (1984). We believe that our path is physically more reasonable.

Using the above relations, the physical quantities at the intermediate states are determined as

$$c_{j+1/3} = \frac{1}{2}\{(\gamma-1)(u_j - u_{j+1}) + 2(c_j + c_{j+1})\} / \{1 + (s_{j+1}/s_j)^{1/2\gamma}\} \tag{3.16}$$

$$\rho_{j+1/3} = (c_{j+1/3}^2/\gamma s_j)^{1/(\gamma-1)} \tag{3.17}$$

$$u_{j+1/3} = u_j + 2(c_j - c_{j+1/3})/(\gamma-1) \tag{3.18}$$

$$u_{j+2/3} = u_{j+1/3} \tag{3.19}$$

$$c_{j+2/3} = c_{j+1/3} - \frac{1}{2}(\gamma-1)(u_{j+1} - u_{j+2/3}) \tag{3.20}$$

$$\rho_{j+2/3} = (c_{j+2/3}^2/\gamma s_{j+1})^{1/(\gamma-1)} \tag{3.21}$$

where $s = p/\rho^\gamma$ is the entropy function.

Once the intermediate states are known, each eigen-value at the grid or intermediate state can be computed. Then, the integral reduces to the sum of Eqs. (3.10), (3.11) and (3.12), following the signs of the eigen-values.

$$\begin{aligned}\int_{\lambda_i<0} A d\boldsymbol{Q} = {} & (\boldsymbol{E}(\boldsymbol{Q}_{j+1/3}) - \boldsymbol{E}(\boldsymbol{Q}_j)) && \text{if } \lambda_1 = u - c < 0 \\ & + (\boldsymbol{E}(\boldsymbol{Q}_{j+2/3}) - \boldsymbol{E}(\boldsymbol{Q}_{j+1/3})) && \text{if } \lambda_2 = u < 0 \\ & + (\boldsymbol{E}(\boldsymbol{Q}_{j+1}) - \boldsymbol{E}(\boldsymbol{Q}_{j+2/3})) && \text{if } \lambda_3 = u + c < 0\end{aligned} \tag{3.22}$$

Because of the non-linearity of the equations, the eigen-values may not be constant along the subpath. The eigen-values λ_1 and λ_3 can change their signs along the subpaths, while the eigen-value λ_2 does not. When λ_1 and/or λ_3 change their signs, the sonic point, where the relevant eigen-value vanishes, arises on the corresponding subpath. Denoting the sonic points on the subpath $L1$ to be $\boldsymbol{Q}_{j+1/6}$ and

on the subpath $L3$ to be $\boldsymbol{Q}_{j+5/6}$, they can be calculated by using the Riemann invariants and the sonic relation as

$$c_{j+1/6}=u_{j+1/6}=\frac{\gamma-1}{\gamma+1}\left(u_j+\frac{2}{\gamma-1}c_j\right) \tag{3.23}$$

$$\rho_{j+1/6}=(c^2_{j+1/6}/\gamma s_j)^{1/(\gamma-1)} \tag{3.24}$$

$$-c_{j+5/6}=u_{j+5/6}=\frac{\gamma-1}{\gamma+1}\left(u_{j+1}-\frac{2}{\gamma-1}c_{j+1}\right) \tag{3.25}$$

$$\rho_{j+5/6}=(c^2_{j+5/6}/\gamma s_{j+1})^{1/(\gamma-1)} \tag{3.26}$$

Thus, the total fluxes are written in the following form

$$\begin{aligned}\boldsymbol{E}_{j+1/2}&=\boldsymbol{E}(\boldsymbol{Q}_j)+\int_{\lambda_i<0}A d\boldsymbol{Q}\\&=\boldsymbol{E}(\boldsymbol{Q}_j)\\&\quad+(\boldsymbol{E}(\boldsymbol{Q}_{j+1/3})-\boldsymbol{E}(\boldsymbol{Q}_j)) \quad \text{if } u_{j+1/3}-c_{j+1/3}<0 \text{ and } u_j-c_j<0\\&\quad+(\boldsymbol{E}(\boldsymbol{Q}_{j+1/6})-\boldsymbol{E}(\boldsymbol{Q}_j)) \quad \text{if } u_{j+1/3}-c_{j+1/3}\geqq 0 \text{ and } u_j-c_j<0\\&\quad+(\boldsymbol{E}(\boldsymbol{Q}_{j+1/3})-\boldsymbol{E}(\boldsymbol{Q}_{j+1/6})) \quad \text{if } u_{j+1/3}-c_{j+1/3}<0 \text{ and } u_j-c_j\geqq 0\\&\quad+(\boldsymbol{E}(\boldsymbol{Q}_{j+2/3})-\boldsymbol{E}(\boldsymbol{Q}_{j+1/3})) \quad \text{if } u_{j+1/3}=u_{j+2/3}<0\\&\quad+(\boldsymbol{E}(\boldsymbol{Q}_{j+1})-\boldsymbol{E}(\boldsymbol{Q}_{j+2/3})) \quad \text{if } u_{j+2/3}+c_{j+2/3}<0 \text{ and } u_{j+1}+c_{j+1}<0\\&\quad+(\boldsymbol{E}(\boldsymbol{Q}_{j+1})-\boldsymbol{E}(\boldsymbol{Q}_{j+5/6})) \quad \text{if } u_{j+2/3}+c_{j+2/3}\geqq 0 \text{ and } u_{j+1}+c_{j+1}<0\\&\quad+(\boldsymbol{E}(\boldsymbol{Q}_{j+5/6})-\boldsymbol{E}(\boldsymbol{Q}_{j+2/3})) \quad \text{if } u_{j+2/3}+c_{j+2/3}<0 \text{ and } u_{j+1}+c_{j+1}\geqq 0\end{aligned} \tag{3.27}$$

The Osher scheme gives a numerical flux between two constant states $\boldsymbol{Q}_j$ and $\boldsymbol{Q}_{j+1}$ which is an approximation of the Riemann flux. Consider a Riemann problem in which the initial value of the dependent variables at the each side of the boundary are constant. The variables at the left are denoted by the subscript j, while those at the right by $j+1$. Instead of using the exact solution for this Riemann problem, an approximate solution using the simple wave is applicable. In the exact solution, a rarefaction-wave, contact-surface and shock-wave can appear generally. In our approximation, the shock-wave is approximated by a compression wave.

Using the Riemann invariants, the relationships between the states are given by Eq. 3. (13-15), and the value of the variables at the boundary are determined by following the signs of eigen-values. If the variables at the boundary are denoted by subscript 'b',

$$\begin{aligned}&\boldsymbol{Q}_b=\boldsymbol{Q}_j \quad \text{if } u-c\geqq 0\\&\boldsymbol{Q}_b=\boldsymbol{Q}_{1/3} \quad \text{if } u-c<0 \text{ and } u\geqq 0\\&\boldsymbol{Q}_b=\boldsymbol{Q}_{2/3} \quad \text{if } u<0 \text{ and } u+c\geqq 0\\&\boldsymbol{Q}_b=\boldsymbol{Q}_{j+1} \quad \text{if } u+c<0\end{aligned} \tag{3.28}$$

The fluxes at the boundary are

$$\begin{aligned}\boldsymbol{E}_b&=\boldsymbol{E}(\boldsymbol{Q}_j)\\&\quad+(\boldsymbol{E}(\boldsymbol{Q}_{1/3})-\boldsymbol{E}(\boldsymbol{Q}_j) \quad \text{if } u-c<0 \text{ and } u\geqq 0\end{aligned}$$

$$+(\boldsymbol{E}(\boldsymbol{Q}_{2/3})-\boldsymbol{E}(\boldsymbol{Q}_{1/3}) \quad \text{if } u<0 \text{ and } u+c\geqq 0$$
$$+(\boldsymbol{E}(\boldsymbol{Q}_{j+1})-\boldsymbol{E}(\boldsymbol{Q}_{2/3}) \quad \text{if } u+c<0 \tag{3.29}$$

If a rarefaction wave is on the boundary, the values at the sonic point, where $u-c$ or $u+c$ vanishes, should be adopted. After all, these fluxes are equivalent to the numerical fluxes used in the Osher scheme. Thus, the Osher scheme is regarded as the approximate Riemann problem solver using simple waves.

4. The Osher scheme for generalized curvilinear coordinate

Next, we consider a two dimensional case; an extension to three dimension is straightforward. The two-dimensional form of the unsteady Euler equations in the Cartesian coordinate system is written as

$$\boldsymbol{Q}_t+\boldsymbol{E}_x+\boldsymbol{F}_y=0 \tag{4.1}$$

where

$$\boldsymbol{Q}=(\rho,\ \rho u,\ \rho v,\ e)^T \tag{4.2}$$
$$\boldsymbol{E}=(\rho u,\ \rho u^2+p,\ \rho uv,\ (e+p)u)^T \tag{4.3}$$
$$\boldsymbol{F}=(\rho v,\ \rho uv,\ \rho v^2+p,\ (e+p)v)^T \tag{4.4}$$

The equation (4.1) can be written in a quasi-linear form as

$$\boldsymbol{Q}_t+A\boldsymbol{Q}_x+B\boldsymbol{Q}_y=0 \tag{4.5}$$

where

$$A=\partial\boldsymbol{E}/\partial\boldsymbol{Q},\ B=\partial\boldsymbol{F}/\partial\boldsymbol{Q} \tag{4.6}$$

are Jacobians.

Let us introduce a generalized transformation of coordinate:

$$\xi=\xi(x,\ y)$$
$$\eta=\eta(x,\ y) \tag{4.7}$$

We have a transformation Jacobian, J, defined as

$$J=\xi_x\eta_y-\eta_x\xi_y=1/(x_\xi y_\eta-x_\eta y_\xi) \tag{4.8}$$

The metrics are numerically computed using the following relation:

$$\xi_x=Jy_\eta,\ \xi_y=-Jx_\eta,$$
$$\eta_x=-Jy_\xi,\ \eta_y=Jx_\xi \tag{4.9}$$

For later use, we define the contravariant velocities, U and V, defined as

$$U=u\xi_x+v\xi_y$$
$$V=u\eta_x+v\eta_y \tag{4.10}$$

The governing Euler equation (4.1) may then be transformed by the chain-rule differentiation into

$$\boldsymbol{Q}_t+(\xi_x\boldsymbol{E}_\xi+\xi_y\boldsymbol{F}_\xi)+(\eta_x\boldsymbol{E}_\eta+\eta_y\boldsymbol{F}_\eta)=0 \tag{4.11}$$

Since this equation is not in a strong conservation form, it is not suitable for capturing a shock. The strong conservation form can be obtained by using Eqs. (4.8) and (4.9) as

$$\hat{\boldsymbol{Q}}_t+\hat{\boldsymbol{E}}_\xi+\hat{\boldsymbol{F}}_\eta=0 \tag{4.12}$$

where

$$\hat{\boldsymbol{Q}}=\frac{1}{J}\boldsymbol{Q}=\frac{1}{J}(\rho,\ \rho u,\ \rho v,\ e)^T \tag{4.13}$$

$$\hat{\boldsymbol{E}}=\frac{1}{J}(\xi_x\boldsymbol{E}+\xi_y\boldsymbol{F})$$

$$=\frac{1}{J}(\rho U,\ \rho uU+\xi_x p,\ \rho vV+\xi_y p,\ (e+p)U)^T \tag{4.14}$$

$$\hat{\boldsymbol{F}}=\frac{1}{J}(\eta_x\boldsymbol{E}+\eta_y\boldsymbol{F})$$

$$=\frac{1}{J}(\rho V,\ \rho uV+\eta_x p,\ \rho vV+\eta_y p,\ (e+p)V)^T \tag{4.15}$$

Similar to Eq. (3.8), we define the numerical flux functions in each coordinate direction as

$$\hat{\boldsymbol{E}}_{i+1/2,j}=\hat{\boldsymbol{E}}_{i,j}+\int_{\lambda_k<0}\hat{A}d\boldsymbol{Q}$$

$$\hat{\boldsymbol{F}}_{i,j+1/2}=\hat{\boldsymbol{F}}_{i,j}+\int_{\lambda_l<0}\hat{B}d\boldsymbol{Q} \tag{4.16}$$

in which $\hat{A}$ and $\hat{B}$ are the Jacobian matrices of the flux functions $\hat{\boldsymbol{E}}$ and $\hat{\boldsymbol{F}}$ defined as

$$\hat{A}=\partial\hat{\boldsymbol{E}}/\partial\hat{\boldsymbol{Q}},\quad \hat{B}=\partial\hat{\boldsymbol{F}}/\partial\hat{\boldsymbol{Q}} \tag{4.17}$$

Here, let us consider the ξ derivatives. The η derivatives can be treated in a similar manner. The Jacobian matrix $\hat{A}$ has four eigen-values such as

$$\lambda_1=U-ck_n,\quad \lambda_2=\lambda_3=U,\quad \lambda_4=U+ck_n \tag{4.19}$$

where k_n represents the geometrical scaling factor defined as

$$k_n=(\xi_x^2+\xi_y^2)^{1/2} \tag{4.20}$$

Corresponding to these four eigen-values, we have four linearly independent right eigen-vectors.

Associated with these four eigen-vectors, we can form the integral path made up by three subpaths in the $\boldsymbol{Q}$ space which is now four dimensional. Two intermediate points $\boldsymbol{Q}_{i+1/3,j}$ and $\boldsymbol{Q}_{i+2/3,j}$ can be determined by using the Riemann invariants summarized below:

$$\begin{aligned}&\text{for } \lambda_1=U-ck_n,\ p/\rho^\tau,\ U+2ck_n/(\gamma-1),\ \hat{v}\\ &\text{for } \lambda_2=\lambda_3=U,\ p,\ U\\ &\text{for } \lambda_4=U+ck_n,\ p/\rho^\tau,\ U-2ck_n/(\gamma-1),\ \hat{v}\end{aligned} \tag{4.21}$$

where $\hat{v}$ is a contravariant velocity component on the ξ=constant line:

$$\hat{v}=u\xi_y-v\xi_x \tag{4.22}$$

These Riemann invariants give eight relations for eight unknowns of two intermediate states, and can be solved analytically. If any sonic points occur, the corresponding subpaths must be divided into two parts to account for the upwind feature

properly.

5. Cell Method

In this section we will consider the Euler equation including a source term in three space dimension:

$$\boldsymbol{Q}_t+\boldsymbol{E}_x+\boldsymbol{F}_y+\boldsymbol{G}_z+\boldsymbol{S}=0 \tag{5.1}$$

This equation can be written in the integral form as

$$\int_\Omega \boldsymbol{Q}_t dv+\int_{\partial\Omega}(n_1\boldsymbol{E}+n_2\boldsymbol{F}+n_3\boldsymbol{G})ds+\int_\Omega \boldsymbol{S}dv=0 \tag{5.2}$$

for a fixed region Ω (a cell) with the boundary $\partial\Omega$ (a cell surface). The vector (n_1, n_2, n_3) is a unit outward vector normal to the boundary. If we assume that variables are constant in each cell, Eq. (5.2) can be approximated as

$$\begin{aligned}(A_{i,j,k}\partial\boldsymbol{Q}_{i,j,k}/\partial t)&+h_{i,j+1/2,k}\bar{\boldsymbol{E}}_{i,j+1/2,k}+h_{i,j-1/2,k}\bar{\boldsymbol{E}}_{i,j-1/2,k}\\&+h_{i+1/2,j,k}\bar{\boldsymbol{E}}_{i+1/2,j,k}+h_{i-1/2,j,k}\bar{\boldsymbol{E}}_{i-1/2,j,k}\\&+h_{i,j,k+1/2}\bar{\boldsymbol{E}}_{i,j,k+1/2}+h_{i,j,k-1/2}\bar{\boldsymbol{E}}_{i,j,k-1/2}\\&+A_{i,j,k}\boldsymbol{S}_{i,j,k}=0\end{aligned} \tag{5.3}$$

where A is the volume of the cell, h is the area of the side of the cell and $\bar{\boldsymbol{E}}$ is the flux normal to the boundary defined as

$$\bar{\boldsymbol{E}}=n_1\boldsymbol{E}+n_2\boldsymbol{F}+n_3\boldsymbol{G} \tag{5.4}$$

If we compute the flux $\bar{\boldsymbol{E}}$ by using the Osher scheme, we obtain a finite-volume (or integral) version of the Osher scheme. Though the finite-volume version may look different from finite-difference version, the procedures are almost equivalent. The major differences between the two versions are in the calculation of the metrics and the Jacobian of the transformation.

In the finite-difference version, the variables and a grid point are defined at the same point, and the metrics and the Jacobian are calculated by using central difference formulas. However, in the finite-volume version, the variables and a grid point are defined at a staggered point. Then, we calculate the area and the normal unit vector of the cell-interface and the volume of the cell (or length and area in two-dimension), rather than the metrics and the Jacobian. The normal unit vectors multiplied by the area of a cell interface and the volume of a cell are equivalent to the metrics and the Jacobian.

Another difference is the treatment of the boundary condition. In the finite-difference version, the dependent variables are defined on the boundaries such as a rigid body or an outer boundary. On the other hand, in the finite-volume version we define the fluxes on the boundary, and the variables nearest to the boundary are departed for a half mesh size.

For the explanation of the cell method, it is convenient to introduce the local Cartesian coordinate system in which one coordinate line is normal to the cell inter-

face. Consider a Riemann problem which has a 3-dimensional velocity field. The intermediate states denoted by the subscript, 1/3 or 2/3, are introduced. Let u be the velocity component normal to the cell interface, and v, w tangential the cell interface. For this case, the characteristic velocities are $u-c$, u, and $u+c$. Using the Riemann invariants for the 3-dimensional Euler equation, the relations between each state are given by

$$
\begin{aligned}
&u_{i,j}+2c_{i,j}/(\gamma-1)=u_{1/3}+2c_{1/3}/(\gamma-1)\\
&p_{i,j}/\rho_{i,j}^{\gamma}=p_{1/3}/\rho_{1/3}^{\gamma}\\
&v_{i,j}=v_{1/3}\\
&w_{i,j}=w_{1/3} \qquad (5.5)\\
&p_{1/3}=p_{2/3},\ u_{1/3}=u_{2/3} \qquad (5.6)\\
&u_{2/3}-2c_{2/3}/(\gamma-1)=u_{i,j+1}-2c_{i,j+1}/(\gamma-1)\\
&p_{2/3}/\rho_{2/3}^{\gamma}=p_{i,j+1}/\rho_{i,j+1}^{\gamma}\\
&v_{2/3}=v_{i,j+1}\\
&w_{2/3}=w_{i,j+1} \qquad (5.7)
\end{aligned}
$$

In this framework a contravariant velocity is regarded as the velocity component normal to the cell interface.

In an axisymmetric case special attention should be paid. Consider that i, j and k represent the axial, the radial and the azimuthal direction, respectively. Let us assume that the azimuthal velocity is absent. In this case, the mass flux and the energy flux through the interfaces at $(i,\ j,\ k+1/2)$ and $(i,\ j,\ k-1/2)$ vanish, and only the momentum flux by the pressure remains.

$$
\begin{aligned}
(A_{i,j,k}\partial \boldsymbol{Q}_{i,j,k}/\partial t)&+h_{i,j+1/2,k}\bar{\boldsymbol{E}}_{i,j+1/2,k}+h_{i,j-1/2,k}\bar{\boldsymbol{E}}_{i,j-1/2,k}\\
&+h_{i+1/2,j,k}\bar{\boldsymbol{E}}_{i+1/2,j,k}+h_{i-1/2,j,k}\bar{\boldsymbol{E}}_{i-1/2,j,k}\\
&+h_{i,j,k+1/2}\bar{\boldsymbol{E}}'_{i,j,k+1/2}+h_{i,j,k-1/2}\bar{\boldsymbol{E}}'_{i,j,k-1/2}\\
&+A_{i,j,k}\boldsymbol{S}_{i,j,k}=0 \qquad (5.8)
\end{aligned}
$$

where

$$\boldsymbol{E}'=n_1(0,\ p,\ 0,\ 0,\ 0)^T+n_2(0,\ 0,\ p,\ 0,\ 0)^T+n_3(0,\ 0,\ 0,\ p,\ 0)^T$$

For a 2-dimensional axisymmetric calculation, a 3-dimensional treatment is needless of course. If we consider a small computational cell in an axisymmetric coordinate system, we can take one velocity component in the azimuthal direction and neglect it. Finally, we take the azimuthal angle of the computational cell to be infinitely small, and we obtain the following form

$$
\begin{aligned}
&(r_{i,j,k}A_{i,j,k}\partial \boldsymbol{Q}_{i,j,k}/\partial t)\\
&\quad+r_{i,j+1/2,k}h_{i,j+1/2,k}\bar{\boldsymbol{E}}_{i,j+1/2,k}+r_{i,j-1/2,k}h_{i,j-1/2,k}\bar{\boldsymbol{E}}_{i,j-1/2,k}\\
&\quad+r_{i+1/2,j,k}h_{i+1/2,j,k}\bar{\boldsymbol{E}}_{i+1/2,j,k}+r_{i-1/2,j,k}h_{i-1/2,j,k}\bar{\boldsymbol{E}}_{i-1/2,j,k}\\
&\quad+A_{i,j,k}(r_{i,j,k}\boldsymbol{S}_{i,j,k}+p_{i,j,k})=0 \qquad (5.9)
\end{aligned}
$$

where A and h are the area of the cell and the length of the cell interface for a 2-

dimensional calculation, and r is the distance from the axis.

A special treatment for the axial singularity is needless, since the area of the boundary interface at the axis merely vanishes and the flux is taken to be zero there.

6. Second order accurate scheme

In the first order Osher scheme, the numerical flux between j-th cell and the $j+1$-th cell is calculated by using the dependent variable at the cell center itself. From the meaning of the Riemann problem, that corresponds to the assumption that the dependent variables in a cell are constant. Even in a smooth region, such an assumption makes $O(\Delta x)$ jumps of variables at the boundary, and it produces a spurious entropy increase. To construct a higher order scheme, we must introduce some structures inside the cell. van Leer (1979) and van Albada et al. (1982) introduced a piece-wise linear distribution in each cell, and we follow their line. Denoting the first and the second derivatives to be $d\boldsymbol{Q}/dx$ and $d^2\boldsymbol{Q}/dx^2$ respectively, the gradient of each variable in the cell can be computed by the averaging function as

$$\begin{aligned}\boldsymbol{Q}'_j &= ((b^2+c)a+(a^2+c)b)/(a^2+b^2+2c)\\ &= (d\boldsymbol{Q}/dx)_j+O(\Delta x^2)\end{aligned} \tag{6.1}$$

where

$$\begin{aligned}a &= (\boldsymbol{Q}_{j+1}-\boldsymbol{Q}_j)/\Delta x\\ &= (d\boldsymbol{Q}/dx)_{j+1/2}+O(\Delta x^2)\\ &= (d\boldsymbol{Q}/dx)_j+(d^2\boldsymbol{Q}/dx^2)_j\frac{\Delta x}{2}+O(\Delta x^2)\end{aligned} \tag{6.2}$$

$$\begin{aligned}b &= (\boldsymbol{Q}_j-\boldsymbol{Q}_{j-1})/\Delta x\\ &= (d\boldsymbol{Q}/dx)_{j-1/2}+O(\Delta x^2)\\ &= (d\boldsymbol{Q}/dx)_j-(d^2\boldsymbol{Q}/dx^2)_j\frac{\Delta x}{2}+O(\Delta x^2)\end{aligned} \tag{6.3}$$

Here, c is a small positive number introduced to avoid division by zero. Using the numerical flux function calculated by the first order Osher scheme and the gradient in (6.1), the flux for the second order scheme at the boundary $j+1/2$ can be defined as

$$\hat{\boldsymbol{E}}_{j+1/2}=\hat{\boldsymbol{E}}(\boldsymbol{Q}_L,\ \boldsymbol{Q}_R) \tag{6.4}$$

where

$$\begin{aligned}\boldsymbol{Q}_L &= \boldsymbol{Q}_j+\boldsymbol{Q}'_j\frac{\Delta x}{2}\\ \boldsymbol{Q}_R &= \boldsymbol{Q}_{j+1}-\boldsymbol{Q}'_{j+1}\frac{\Delta x}{2}\end{aligned} \tag{6.5}$$

The piece-wise linear distribution reduces the jumps at the cell boundary to $O(\Delta x^3)$.

In order to apply this procedure to the multidimensional general coordinate

system, the Cartesian coordinate x should be replaced by general coordinates, and the gradients should be defined for each direction in the general coordinate.

The second order of accuracy in time can be achieved by adopting the multi step procedure. Let us consider the following equation with the source term:

$$Q_t+E_x+H=0 \tag{6.6}$$

At the first step the source term is integrated to advance the half timestep as

$$Q_j^1=Q_j^n-\frac{\Delta t}{2}H_j^n \tag{6.7}$$

Then, using the procedure in Eq. (6.1) to estimate the spatial gradient, we can advance the time to $t+\Delta t/2$ as

$$\begin{aligned} Q_j^2&=Q_j^1+\frac{\Delta t}{2}(\partial Q^1/\partial t)_j \\ &=Q_j^1-\frac{\Delta t}{2}(AQ_j^{1\prime}) \end{aligned} \tag{6.8}$$

in which the contribution from the source term is omitted. The dependent variables at the cell boundaries can be estimated as

$$\begin{aligned} Q_L^2&=Q_j^2+\frac{\Delta x}{2}Q_j^{1\prime} \\ Q_R^2&=Q_{j+1}^2-\frac{\Delta x}{2}Q_{j+1}^{1\prime} \end{aligned} \tag{6.9}$$

We can form the numerical flux function of Eq. (6.4) and can advance the time to $t+\Delta t$ by the time centered integration formula to keep the second order of accuracy in time as

$$Q_j^3=Q_j^1-\frac{\Delta t}{\Delta x}(E_{j+1/2}^2-E_{j-1/2}^2) \tag{6.10}$$

To complete the integration, we must account for the rest of the contribution of the source term as

$$Q_j^{n+1}=Q_j^3-\frac{\Delta t}{2}H_j^3 \tag{6.11}$$

In a scalar equation such as Eq. (2.1), this procedure is sufficient. However, in a vector equation such as Eq. (6.6), some problems arise at the intermediate stages (6.8) and (6.9). If we choose the conservative variables such as Eq. (3.2) as the dependent variables, an instability can occur. In order to avoid this difficulty, van Albada et al. (1982) used non-conservative quantities such as $\boldsymbol{Q}=(\rho,\ u,\ p)^T$. Since u and p are continuous across a contact surface, this procedure yields smoother intermediate quantities.

7. Numerical implementation of the boundary conditions

1) The inflow and outflow boundaries

Consider a one dimensional problem for the sake of simplicity. The number of

variables, which can be determined at the boundary, depends on the number of characteristics that come into the computational region. In the case of supersonic inflow, three variables can be given at the boundary. In the case of subsonic inflow, two variables can be given, but one is determined by an inner condition. In the case of subsonic outflow, one variable is given and two variables are computed by the inner variables. In the case of supersonic outflow, three variables are computed by the inner variables.

If we introduce imaginary cells next to the boundary, we may give all variables in them to compute the fluxes by the Osher scheme. This procedure gives consistent boundary conditions, since the Osher scheme itself contains the procedure stated above.

2) The rigid (slippery) boundary

In this case, the velocity normal to the boundary should vanish there, and the eigen-value 'u' should be identical to zero. Thus, only one characteristic, e. g. '$u-c$', exists. Using the corresponding Riemann invariants, we have the value of the variables at the boundary as

$$\begin{aligned} u_b &= 0 \\ v_b &= v_n \\ c_b &= c_n + \frac{\gamma-1}{2} u_n \\ \rho_b &= (c_b^2/\gamma s_n)^{1/(\gamma-1)} \end{aligned} \tag{7.1}$$

where the subscript 'n' denotes the variables in the cell next to the boundary, and 'b' denotes those at the boundary.

3) Accreting boundary

We introduce a vacuum cell next to the boundary. For a supersonic outflow, all variables at the boundary are given by those in the cell next to the boundary. If the flow is subsonic, a rarefaction wave appears on the boundary. The eigen-value '$u-c$' vanishes there. Using the Riemann invariants corresponding to the characteristic '$u+c$', the variables at the boundary are given by

$$\begin{aligned} c_b &= u_b \\ &= \frac{\gamma-1}{\gamma+1}\left(u_n + \frac{2}{\gamma-1} c_n\right) \\ v_b &= v_n \\ \rho_b &= (c_b^2/\gamma s_n)^{1/(\gamma-1)} \end{aligned} \tag{7.2}$$

8. Numerical examples

The numerical examples computed are summarized below. We compute an interaction between a gas ejected from a star and an accretion flow onto the star. We also compute an accretion flow about a gravitating solid body.

We use a spherical polar coordinate. The number of meshes in the radial direction is 50 or 100, while that of the circumferential direction is 60. A sphere with a radius r_0 is placed at the center of the numerical domain. Beyond the outer numerical spherical boundary, of which the radius is set to be $130\,r_0$, the uniform flow of gas is assumed. We start the calculation from the state of the uniform flow, i.e. an impulsive start. We follow the time evolution until a steady state is reached, if any exists.

Let us introduce the accretion radius defined as

$$r_a=2Gm/V^2 \tag{8.1}$$

where G, m and V are the gravitational constant, the mass of the body and the speed of gas at the far upstream. A non-dimensional parameter describing the strength of the gravity is

$$\delta=r_a/r_0 \tag{8.2}$$

Another important dimensionless parameter is the Mach number, M, of the upstream gas, which is defined as

$$M=V/c_\infty \tag{8.3}$$

where c_∞ is the sound speed of the upstream gas.

The density and the sound speed of the gas are specified inside the surface of the central sphere. They are denoted as ρ_0 andc_0, respectively. The velocity of the gas is set to be zero in the sphere. The boundary condition at the spherical surface is computed by solving a Riemann problem between the interior state described above and the state just outside of the sphere. Therefore, the speed of gas ejected from or accreted onto the sphere is not necessarily zero.

In the present study, we fix $c_0/c_\infty=5$, and $M=2.4$. It means that the temperature in the star is 25 times more than that at the upstream gas. However, its precise value has no significance for the present problem, since the size of the central sphere is arbitrarily chosen. Two cases of the density ratio ρ_0/ρ_∞ are examined, i.e. 1 and 200. As to δ, we compute two cases, i.e. $\delta=0$ and 10. The former case corresponds to the one in which gravity is not included.

A) THE CASE WITHOUT GRAVITY

We describe the results of the numerical calculations in which gravity is neglected. In Fig. 1, a and b, the result of the calculation for the case with $M=2.4$, $\rho_0/\rho_\infty=200$ and $\gamma=5/3$ are presented. Figure la shows the entropy contours with velocity vectors, while Fig. 1 b shows the density contours. If the flow is steady, the isentropic lines coincide with the stream-lines except at shocks, and we can observe the stream-lines in Fig. 1 a. It can be seen that the contact surface forms a stream-line.

A bow shock is formed at the upstream side of the body, and the inner non-

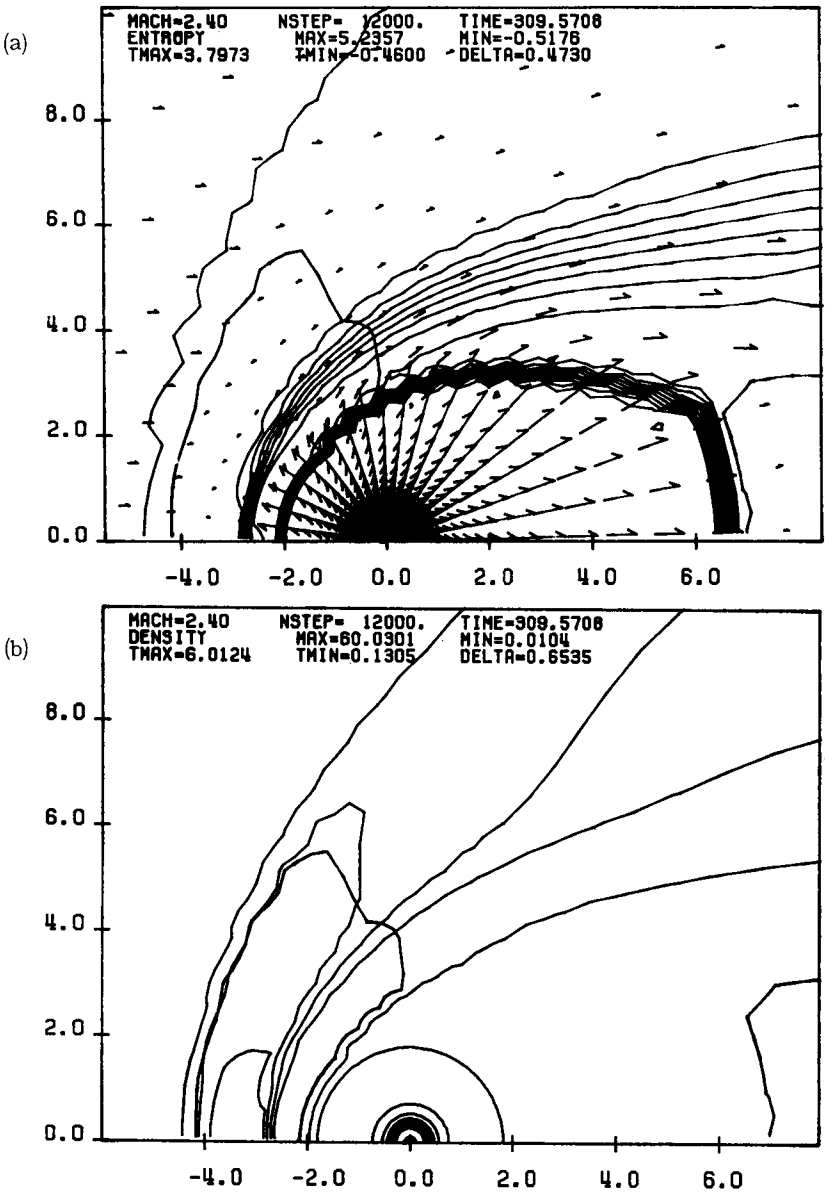

Fig. 1. (a) Entropy contours with velocity vectors, and (b) density contours for the model with the Mach number 2.4, the density ratio 200 and the specific heat ratio 5/3. The gravity is not included. The thick line is the sonic line at which the Mach number is unity. The radius of the central sphere is $0.1\,r_A$. Time is measured in such a unit in which the radius of the central sphere is unity, and the sound speed of the far upstream gas is unity. Therefore, it takes about a 260 time unit for a sound signal to cross the whole numerical domain. *MAX* and *MIN* denote the maximum and the minimum values, respectively, of the physical quantities described. *TMAX* and *TMIN* do those of the contour values. *DELTA* shows a contour spacing.

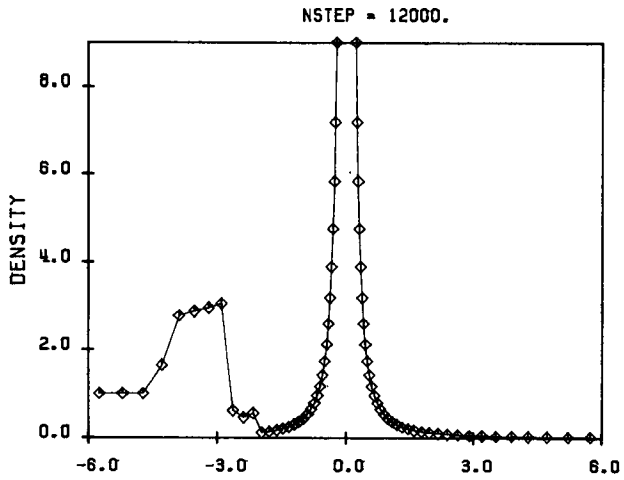

Fig. 2. The density distribution on the symmetry axis. The parameter is the same as in Fig. 1. The contact surface and the inner shock are captured by two mesh points.

spherical shock surrounds the central body. The latter shock is truncated by a plain shock at the rear side of the body. This shape was predicted by Wallis and Dryer (1976). Baranov, Lebedev and Ruderman (1979) computed the same case as ours by the time dependent finite-difference method. They obtained the shape of the shocks and the contact surface only in the leading hemisphere. Our results agree well with theirs.

Figure 2 shows the density distribution of the same model on the symmetry axis. It can be observed that the inner shock and the contact surface are represented by two mesh points, and exhibit neither dissipation nor dispersion errors. As to the bow shock, one transition point lies between the left and right states, and exhibit negligable dissipation errors. This density distribution curve indicates the monotonic property of the present method.

B) THE CASE WITH GRAVITY

Next, we examine the case including gravity. The accretion radius describing the strength of the gravity is fixed to 10 times that of the central sphere, i.e. $\delta=10$, and also the Mach number is fixed at 2.4. Two cases of the density ratio, i.e. 1 and 200 are examined. In the case of the density ratio 200, we show further two cases with the specific heat ratio, $\gamma=4/3$ and 2.

Figure 3, a and b show the entropy and density contours for the case of $\rho_0/\rho_\infty=200$ and $\gamma=5/3$. A comparison of these figures with Fig 1, a and b, shows that the inner shock is pushed into the body, and the supersonic bubble does not exist any more. The gas flows out subsonically from the body. Figure 4 shows the density

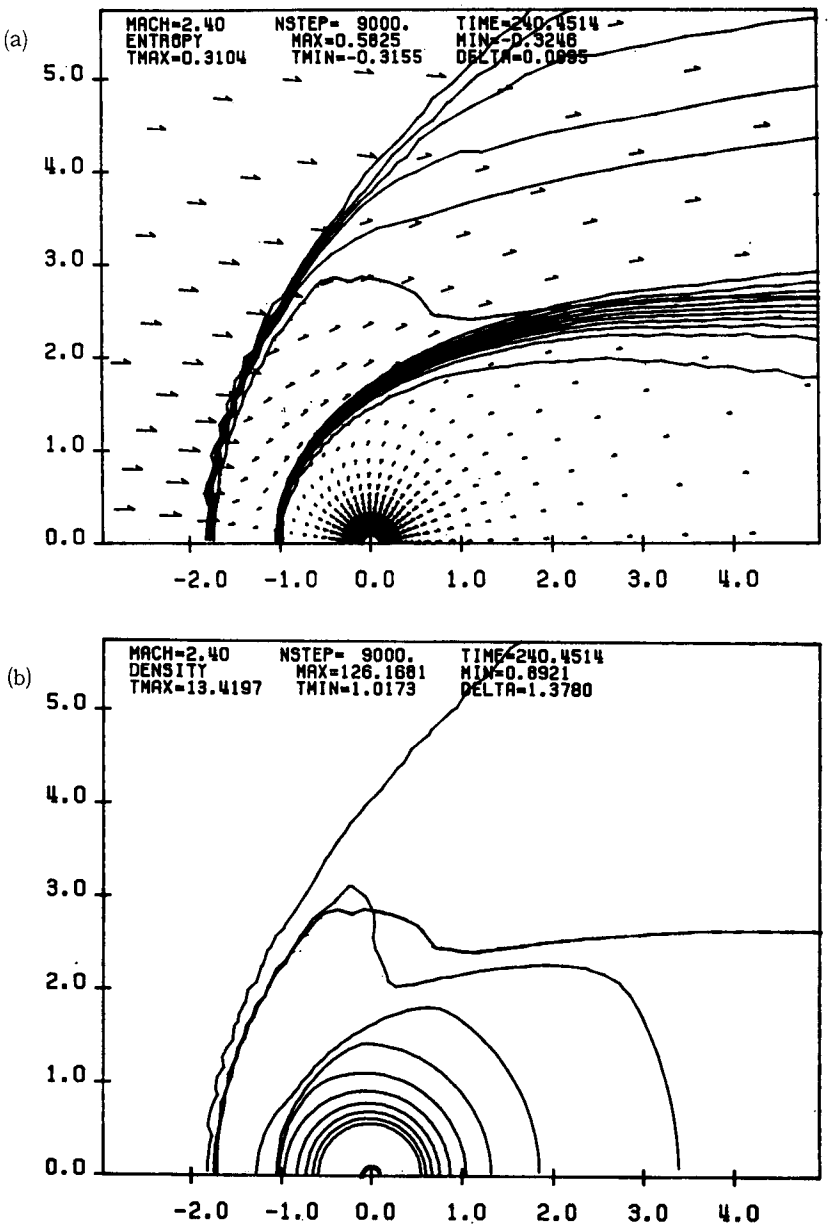

Fig. 3. (a) Entropy contours with velocity vectors, and (b) the density contours for the Mach number 2.4, the density ratio 200 and the specific ratio 5/3. The accretion radius is ten times that of the body radius, i.e. $\delta=10$. The inners shock is pushed into the body, and the supersonic bubble does not exist any more.

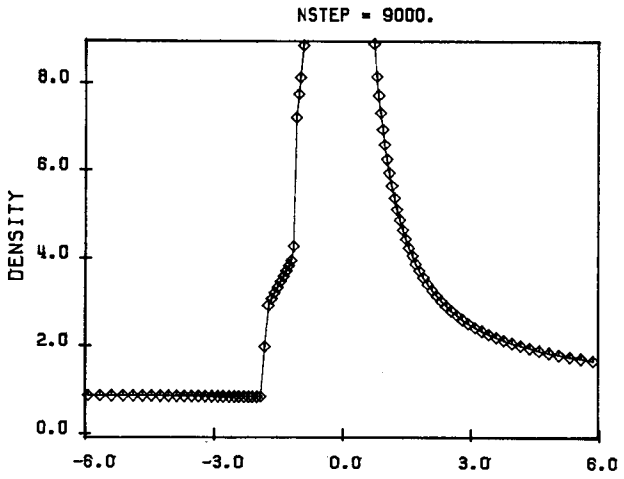

Fig. 4. The density distribution on the symmetry axis. The parameter is the same as in Fig. 3. The accretion flow strips the gas emitted from the spherical body off downstream.

distribution on the axis. The accretion flow blows the gas emitted from the central body off downstream. The bow shock is sharply captured.

Figure 5, a and b represent the entropy and the density contours for the case of $\rho_0/\rho_\infty=200$ and $\gamma=2$. When the specific heat ratio is 2, the mass loss from the body becomes negligible, and an atmosphere surrounding the body is formed. The gas accreting onto the body flows by the atmosphere.

Figure 6, a and b represent the entropy and the density contours for the case of $\rho_0/\rho_\infty=200$ and $\gamma=4/3$. The contact surface shows a wavy nature. Figure 7 shows the density distribution on the symmetry axis. One can see that the slope between the bow shock and the contact surface is sharper than that in Fig. 2. It can be seen that the contact surface is Rayleigh-Taylor unstable. The density of the gas outside of the contact surface is higher than that of the inside.

Taking the accretion radius as a typical length and c_∞ as a typical velocity, we can define a typical time scale as

$$\tau\sim r_a/c_\infty \tag{8.4}$$

Let us assume that the maximum wave length of a disturbance is the distance from the center of the body to the contact surface measured along the front axis, i.e. the so-called standoff distance. Solving the dispersion relation of the Rayleigh-Taylor instability for compressible fluids, we find that the ratio of the e-folding time of the longest wave is considerably shorter than τ. Therefore, we can conclude that the instability of the contact surface is physical.

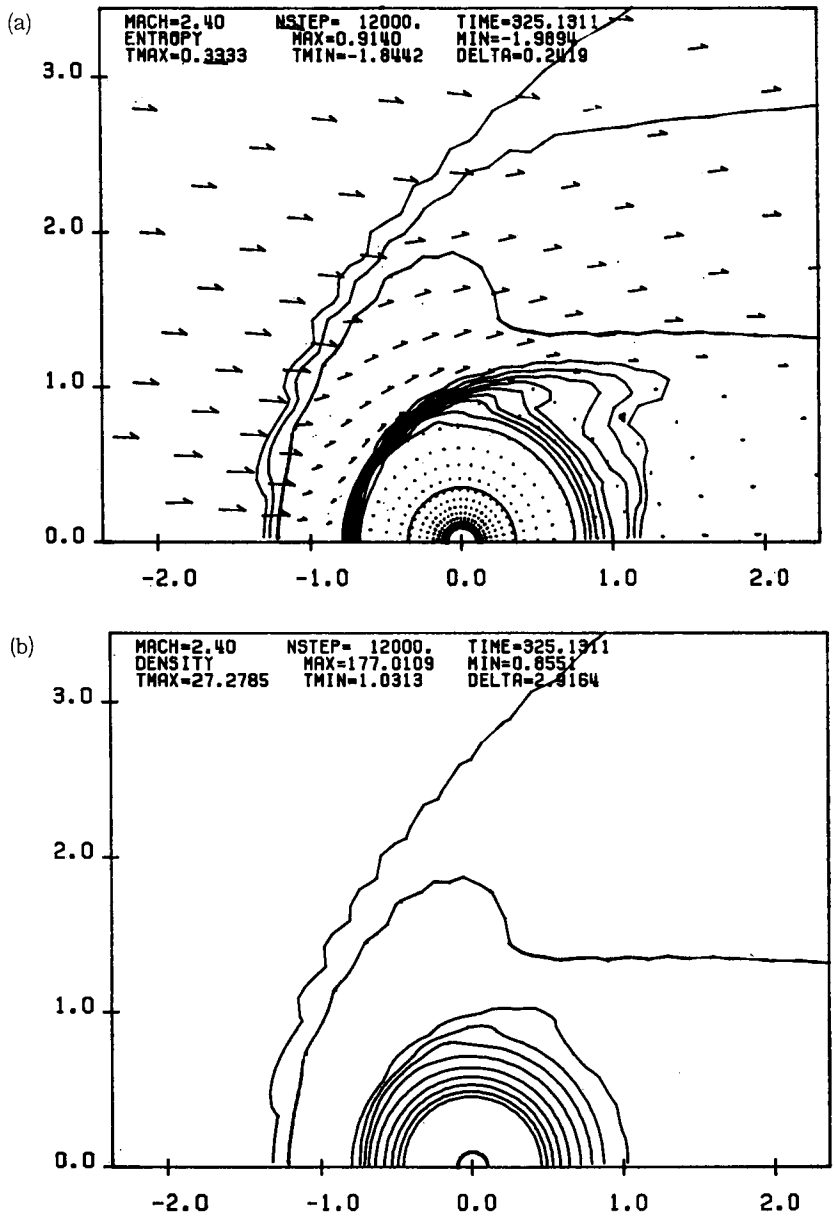

Fig. 5. (a) Entropy contours with velocity vectors, and (b) the density contours for the Mach number 2.4, the density ratio 200 and the specific ratio 2. An atmosphere surrounds the body.

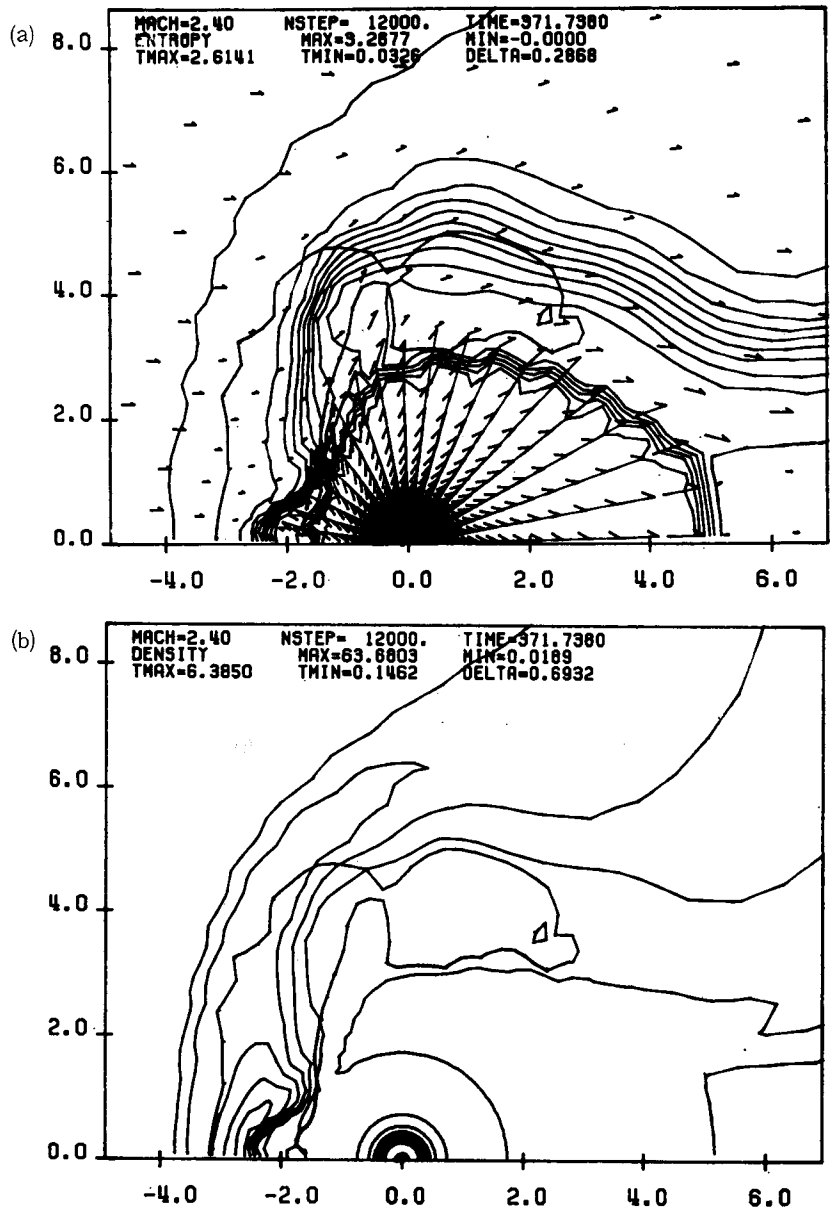

Fig. 6. (a) Entropy contours with velocity vectors, and (b) the density contours for the Mach number 2.4, the density ratio 200 and the specific ratio 4/3. The contact surface shows a wavy nature due to the Rayleigh-Taylor instability.

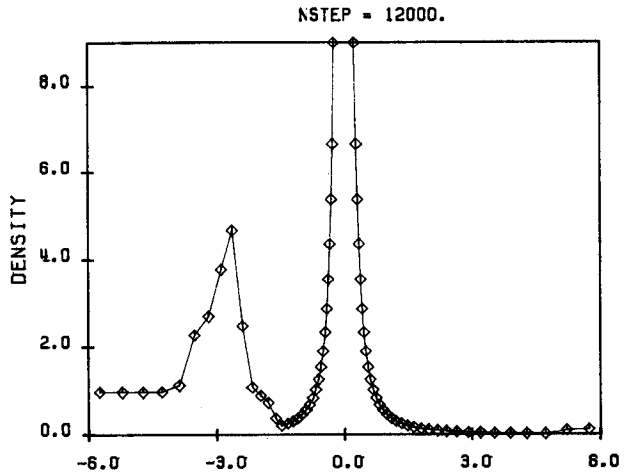

Fig. 7. The density distribution on the symmetry axis. The parameter is the same as in Fig. 6. The slope between the bow shock and the contact surface is sharper than that in Fig. 2.

Figure 8, a and b show the entropy and the density contours for the case of $\rho_0/\rho_\infty=1$, respectively. This case exhibits the accretion flow. These calculations have been done for the same Mach number and the same specific heat ratio as Hunt (1971). As is shown in Hunt's calculation, this flow also possesses a bow shock. As gas is drawn gravitationally toward the gravitational source, it becomes denser, and creates pressure forces. It is these pressure forces that support the shock. Behind the bow shock, one finds that some isentropic lines, i.e. streamlines, are drawn toward the gravitational source.

8.2. FLOW ABOUT A GRAVITATING RIGID SPHERE

We compute a flow about a gravitating rigid sphere. The parameters are $M=2.4$, $\delta=10$ and $\gamma=5/3$. Figure 9, a and b show the entropy and the density contours, respectively. We can find the occurrence of a vortex ring about the body. This phenomena is also observed by Takeda, Matsuda, Sawada and Hayashi (1985) for the supersonic Navier Stokes flows, and by Shima, Matsuda, Takeda and Sawada (1985) for the supersonic inviscid flow.

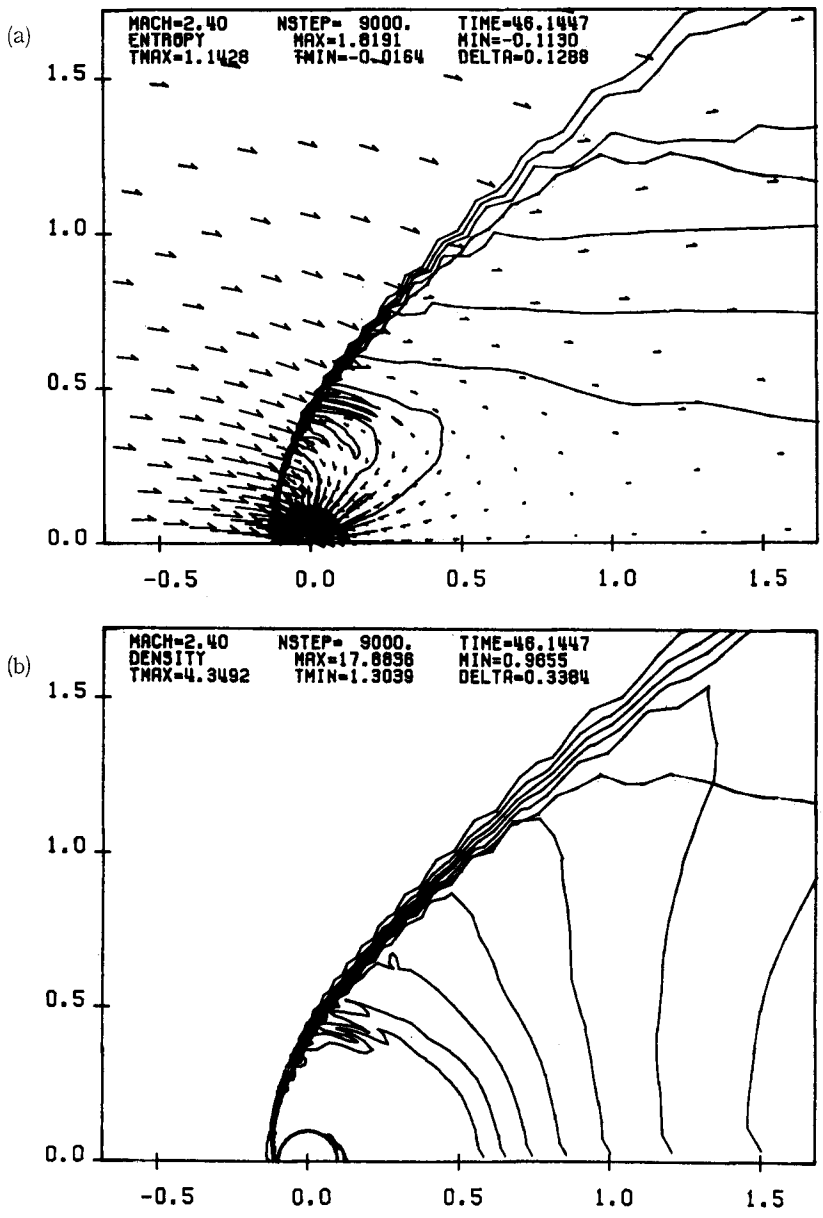

Fig. 8. (a) Entropy contours with velocity vectors, and (b) the density contours for the Mach number 2.4, the density ratio 1 and the specific heat ratio 5/3. The accretion flow occurs.

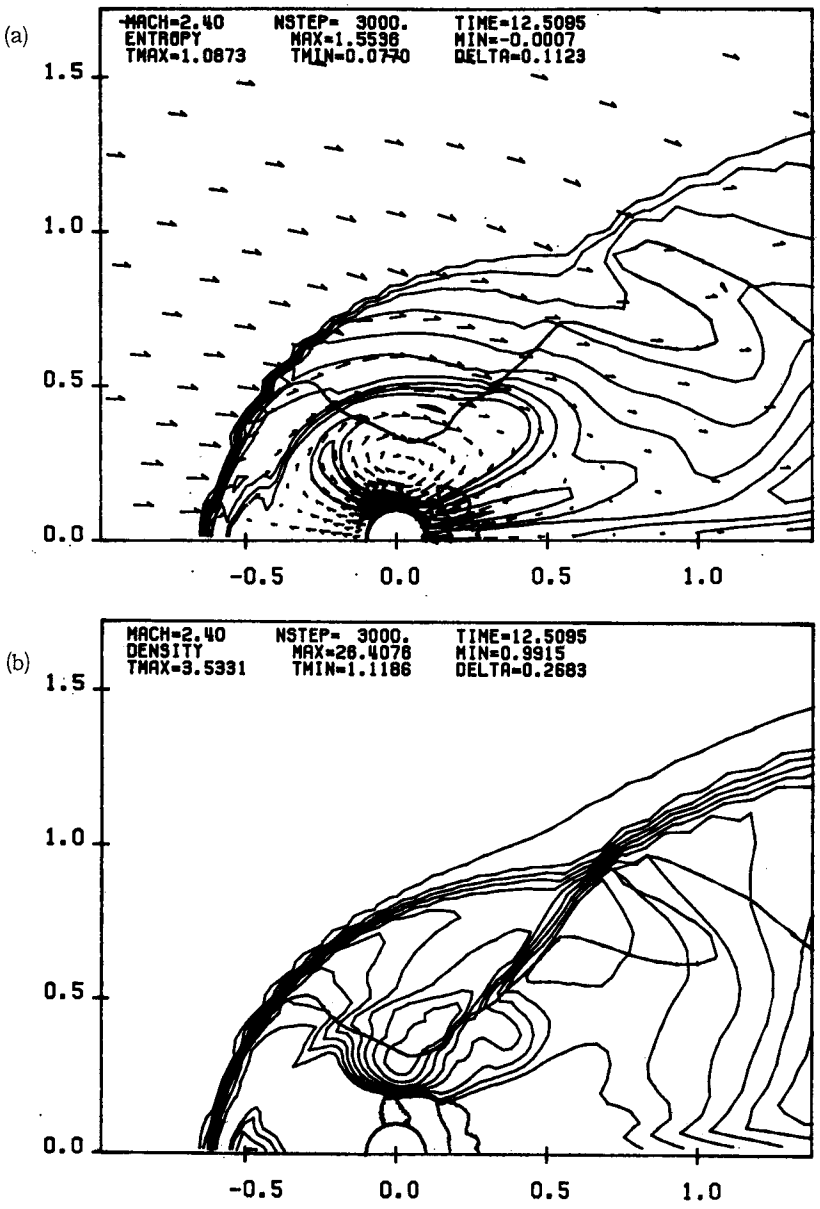

Fig. 9. (a) Entropy contours with velocity vectors, and (b) the density contours for the Mach number 2.4 and the specific heat ratio 5/3. The inner sphere is a solid body. A vortex ring about the body is observed.

References

van Albada, G. D., van Leer, B. & Roberts, W. W. Jr., 1982. Astron. Astrophys., **108**, 76.
Baranov, V. B., Lebedev, M. G. & Ruderman, M. S., 1979. Astrophys. Space Sci., **66**, 441.
Beam, R. M. & Warming, R. F., 1976. J. Comp. Phys., **22**, 87.
Chakravarthy, S. & Osher, S., 1983. AIAA J., **21**, 1241.
Courant, R., Isaacson, E. & Rees, M., 1952. Comm. Pure Appl. Math., **5**, 243.
Godunov, S. K., 1959. Mat. Sbornik, **47**, 271.
Hunt, R., 1971. Mon. Not. R. astr. Soc., **154**, 141.
van Leer, B., 1979. J. Comp. Phys., **32**, 101.
Osher, S. & Chakravarthy, S., 1983. J. Comp. Phys., **50**, 447.
Pandolfi, M., 1984. AIAA J., **22**, 602.
Roe, P. L., 1981. J. Comp. Phys., **43**, 357.
Shima, E., Matsuda, T., Takeda, H. & Sawada, K., 1985. Mon. Not. R. astr. Soc., **217**, 367.
Takeda, H., Matsuda, T., Sawada, K. & Hayashi, C., 1985. Prog. Theor. Phys., **74**, 272.
Wallis, M. K. & Dryer, M., 1976. Astrophys. J., **205**, 895.